Real-time assessment of liver fat content using a filter-based Raman system operating under ambient light through lock-in amplification

Guo, H.; Tikhomirov, A.B.; Mitchell, A.; Alwayn, I.P.J.; Zeng, H.S.; Hewitt, K.C.

Research Article | Vol. 13, No. 10 / 1 Oct 2022 / Biomedical Optics Express 5231
Biomedical Optics EXPRESS

Real-time assessment of liver fat content using a filter-based Raman system operating under ambient light through lock-in amplification

HAO GUO,[1,2] ALEXEY B. TIKHOMIROV,[1] ALEXANDRIA MITCHELL,[1,2] IAN PATRICK JOSEPH ALWAYN,[3] HAISHAN ZENG,[4] AND KEVIN C. HEWITT[1,*]

[1]*Department of Physics and Atmospheric Science, Dalhousie University, 6310 Coburg Road, Halifax, NS B3H 4R2, Canada*
[2]*Department of Medical Physics, Nova Scotia Health Authority, 5820 University Avenue Halifax, NS B3H 1V7, Canada*
[3]*Department of Surgery, Leiden University Medical Center (LUMC) Transplant Center, Albinusdreef 2, 2333 ZA Leiden, The Netherlands*
[4]*Imaging Unit, Integrative Oncology Department, BC Cancer Research Centre, 675 West 10th Avenue, Vancouver, BC V5Z 1L3, Canada*
[*]*Kevin.Hewitt@Dal.ca*

Abstract: During liver procurement, surgeons mostly rely on their subjective visual inspection of the liver to assess the degree of fatty infiltration, for which misclassification is common. We developed a Raman system, which consists of a 1064 nm laser, a handheld probe, optical filters, photodiodes, and a lock-in amplifier for real-time assessment of liver fat contents. The system performs consistently in normal and strong ambient light, and the excitation incident light penetrates at least 1 mm into duck fat phantoms and duck liver samples. The signal intensity is linearly correlated with MRI-calibrated fat contents of the phantoms and the liver samples.

1. Introduction

Liver transplantation gives more than 30,000 patients who suffer from end-stage liver diseases a second chance of life globally every year; however, at the same time, more than 30,000 patients are awaiting a liver transplant (LT) [1,2]. Year after year, thousands of patients on the waiting list die due to a persistent shortage of donor livers. In the meantime, tens of thousands of donor livers are not used for various reasons. In Brazil, 27% of retrieved donor livers were discarded, according to a study from 2015 to 2018 [3]. In the United States, although transplant centres transplanted 90% of retrieved donor livers from 2003 to 2016, they rejected 31% of deceased donor livers before organ procurement [4]. In the United Kingdom, 49% of donor livers were not used from 2018 to 2020 [5], and 39% of discards resulted from fatty liver disease (FLD) [6]. More livers can be transplanted if a quick and accurate method for donor liver fat measurements becomes available.

FLD, also known as hepatic steatosis (HS), has been associated with increased risks of liver graft dysfunction. A liver with more than 5.5% triglyceride content in liver wet weight is identified as a fatty liver [7]. With an increasing prevalence of obesity and non-alcoholic fatty liver disease (NAFLD), HS is becoming the most frequent disorder in liver grafts available for transplantation, especially in Western countries [8,9]. Transplant surgeons are increasingly considering fatty livers eligible for transplantation to lessen the current shortage of donor organ supply [10]. Mild steatosis (5.5%−30%) is usually accepted as safe and has minor impact on the rate of primary nonfunction (PNF) or post-LT outcomes.

#467849 https://doi.org/10.1364/BOE.467849
Journal © 2022 Received 14 Jun 2022; revised 23 Aug 2022; accepted 26 Aug 2022; published 9 Sep 2022

Biomedical Optics EXPRESS

Severe steatosis (>60%) is associated with more risks, and the PNF rate of transplanting these livers is high [10,11]. Meanwhile, outcomes of transplanting moderately (30%–60%) steatotic livers are varying and controversial [12–17]. Transplant surgeons usually make a comprehensive assessment based on the donor's risk factors and the recipient's health conditions to decide whether to accept or reject a donor liver for transplantation. The assessment is performed using the Model For End-Stage Liver Disease (MELD) and the Balance of Risk (BAR) scoring system [18]. Therefore, an accurate assessment of the fat content of moderately fatty livers is the most clinically relevant in the organ procurement stage.

Machine perfusion and defatting strategies bring hope to enlarging the pool of liver grafts with less recipient risk [19]. Recent advances in *ex vivo* normothermic machine perfusion (NMP) offer opportunities to preserve livers under near-physiological conditions and pharmacologically defat macrosteatotic livers [6,20]. However, the lack of accurate metrics to assess the success of liver "rescue" is a significant challenge to the NMP and defatting techniques. The appropriate time to stop the intervention and proceed with the transplant remains to be studied. Measuring triglyceride contents in the perfusate and performing liver biopsies at multiple time points are traditional methods in existing studies [21]; however, these tests are costly, time-consuming, and sometimes invasive to the liver.

The gold standard method to quantify liver fat content is with a liver biopsy conducted by an expert pathologist. However, due to its high cost and resource constraints in local hospitals (i.e., the retrieval sites), only a small proportion of donor livers are assessed by the biopsy during organ retrieval. In most cases of pre-LT assessment during liver procurement, surgeons rely on their subjective visual inspection of the liver to evaluate the degree of fatty infiltration. While most experts can identify livers with mild and severe steatosis based on the macroscopic appearance of the liver [10], many studies indicate an assessment of moderate steatosis is challenging even in experienced hands, and misclassification is common [21,22]. Even if the visual estimation could make a perfect classification of mild, moderate, and severe HS, the fat content range of each category is too large for a reliable risk prediction of fatty donor livers, especially for those with moderate HS.

There are several non-invasive imaging methods to stage HS or quantify liver fat content, including ultrasound (US) imaging, computed tomography (CT), and magnetic resonance imaging (MRI). MRI is recognized as the most accurate non-invasive technique for liver fat quantification, while US and CT are not considered reliable enough [23–25]. However, MRI is not suitable for donors on life-support equipment.

Providing information on the vibrational and rotational states of C-H bonds in triglycerides, Raman spectroscopy (RS) and infrared (IR) spectroscopy open up new opportunities in determining the fat content of donor livers in-situ during organ procurement. Although both RS and IR spectroscopy techniques have demonstrated the ability to measure the content of hepatic fat without sample preparation [26–29], water interference limits the utilization of IR spectroscopy. The water band in Raman spectra is isolated from the spectral features of interest, thus Raman spectra are more suitable for a precise assessment of liver steatosis. Hewitt et al. demonstrated that RS with a 785-nm excitation wavelength could provide rapid fat content assessments, which are highly correlated with the pathologist rating in rodent models [30]. Pacia et al. later confirmed the potential of RS in rapid diagnostics of liver steatosis. They demonstrated that chemometric analysis based on intensities of Raman characteristic peaks at 1000 cm^{-1} to 3200 cm^{-1} and especially within the high wavenumber region ranging from 2800 cm^{-1} to 3200 cm^{-1}, is capable of quantifying HS in mice models [31]. However, previous studies did not investigate the most clinically relevant fat range (20%–60%).

The signal of conventional RS is feeble. Approximately one out of every 10^6 – 10^9 scattered photons is a Raman photon. Consequently, Raman spectrometers are usually bulky because of unavoidable chromatic dispersion elements and high sensitivity photoelectric detectors (e.g., liquid

Biomedical Optics EXPRESS

nitrogen-cooled CCD). They require the data collection to be conducted in a dark environment and relatively complex chemometric analysis, which impedes the clinical application of RS for assessing the fat content of potential donor livers.

As the scattering cross-section for fluorescence processes is an order of magnitude larger than Raman processes, broad-band autofluorescence of biological tissues commonly drowns Raman scattering. One common approach to suppressing autofluorescence is using longer wavelength excitation. Mahadevan-Jansen was the first to report using 1064 nm excitation to provide almost fluorescence-free Raman spectra of organs, including the liver [32].

In this work, we developed a Raman system consisting of a 1064 nm laser, a handheld probe, optical filters, photodiodes, and a lock-in amplifier for real-time assessment of liver fat content. The weak signal of characteristic Raman scattering peaks of lipids/proteins is identified using a sensitive lock-in amplification technique, which allows for accurate detection of weak informative signals in bright LED and ordinary luminescent ambient light. We conducted parallel measurements of duck fat phantoms and duck liver samples using a tabletop FT-Raman spectrometer and our Raman system. As the most accurate technique for liver fat quantification, MRI is used to provide reference fat contents of the phantoms and liver samples.

2. Materials and methods

2.1. Hardware and data collection

2.1.1. Filter-based Raman system

The filter-based Raman system is composed of a handheld probe, a multi-channel wavelength band selection system, and a lock-in amplification system. Figure **1**(c) depicts a schematic of the system. A 1064 nm CW Nd:YVO_4 laser (Model MLL-III-1064, CNI Optoelectronics Tech., Changchun, China) is used as the excitation source. The laser can deliver up to 500 mW of continuous-wave power and has a transistor-transistor-logic input for modulation. A square wave (50% duty cycle) signal from a signal generator is used to modulate the laser beam. We tested square wave signals from 500 Hz to 10000 Hz and found 5600 Hz maximizes the output signal.

The laser beam is guided to the handheld probe [Fig. **1**(a) and **1**(b)] by a multimode optical fibre patch cable (Thorlabs, Newton, NJ, USA) with a 200-μm core diameter and 0.22 numerical aperture (NA). In the excitation path of the probe, a longpass dichroic beam splitter (DBS1) with a cut-on wavelength of 1180 nm (Thorlabs) reflects the 1064-nm beam, and the beam is focused on the surface of a sample. The working distance of the probe is the back focal distance of lens L2 (16.60 mm for 1064-nm light). In the collection path, lenses collect back-scattered light from the illuminated area of the sample, and the DBS1 transmits light with wavelengths longer than 1180 nm, which is coupled into an optical fibre patch cable with a 1000-μm diameter (Thorlabs). This fibre patch cable guides the light to the multi-channel wavelength band selection system, where a longpass filter with a cut-on wavelength of 1400 nm (Thorlabs) further filters the diffuse reflection light at 1064 nm. A shortpass DBS (DBS2) with a cut-on wavelength of 1500 nm (Thorlabs) splits the filtered beam into 1550/30-nm and 1064/3-nm channels.

In the 1550/30-nm channel, Raman scattered light with wavelengths longer than 1500 nm is filtered by a 1550-nm bandpass filter (BPF1) with a full width at half maximum (FWHM) of 30 nm (Chroma Technology, Bellows Falls, VT, USA), then focused onto a 2-mm-in-diameter InGaAs photodiode (D1) with a spectral range of 800-1700nm (Thorlabs). This channel detects signals within 2879 cm^{-1} to 3012 cm^{-1} range in terms of the Raman shift, which covers the symmetric and asymmetric stretching modes of CH_2 and CH_3 in lipids and proteins and the stretching modes of = C-H bonds in lipids [33,34]. The LPF blocks 99.98% of the 1064-nm light, and the 1064/3-nm channel detects the transmitted 0.02%. In the 1064/3-nm channel, the light with wavelengths shorter than 1500 nm is transmitted through DBS1, filtered by a 1064-nm laser

Biomedical Optics EXPRESS

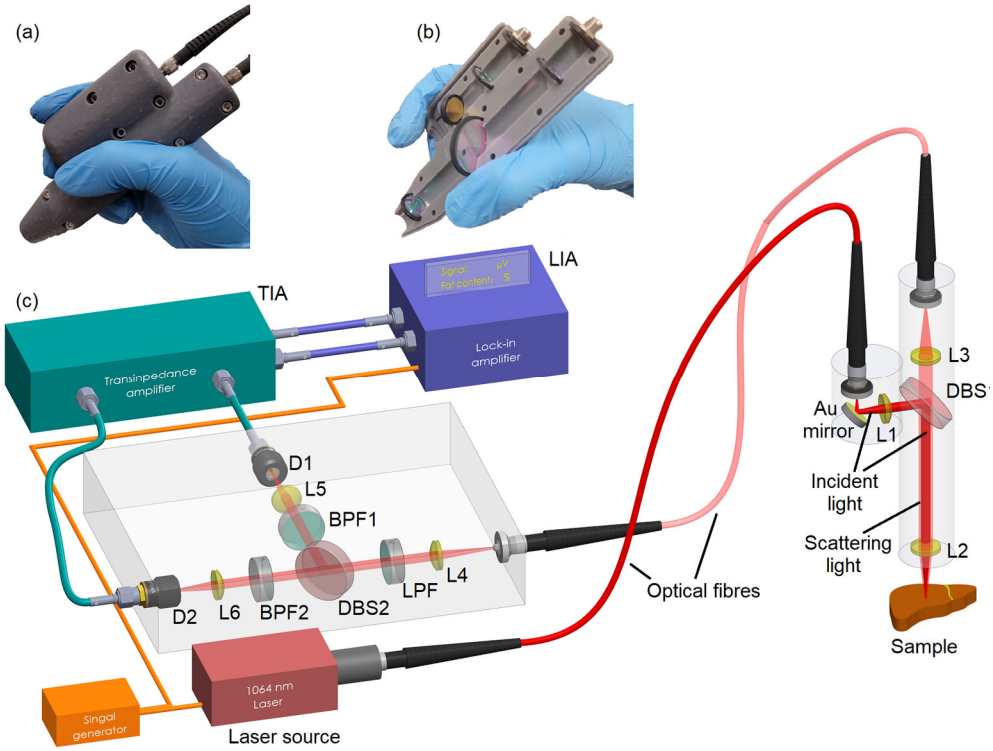

Fig. 1. (a) 1:1 scale handheld probe held in the author's hand. (b) 1:1 scale handheld probe equipped with optical elements. (c) Schematic of the optical filter-based Raman system. L1-L5: lenses; DBS1: 1180-nm longpass dichroic beam splitter; DBS2: 1500-nm shortpass dichroic beam splitter; LPF: 1400-nm longpass filter; BPF1: 1550/30-nm bandpass filter; BPF2: 1064/3-nm laser line filter; D1-D2: InGaAs photodiodes; TIA: transimpedance amplifier; LIA: lock-in amplifier.

line filter with an FWHM of 3 nm (Thorlabs). The filtered light is considered a diffuse reflection of the sample and focused onto an identical InGaAs photodiode (D2).

The lock-in amplifier (LIA) extracts weak Raman signals from the intense noise signals at other frequencies or random phases, which are rejected through filtering. The signal from the LIA is a product of the internal reference signal $V_{ref} = V_r \sin(\omega t + \theta_{ref})$ and the Raman signal $V_{sig} = V_s \sin(\omega t + \theta_{sig})$ from the photodiode:

$$\begin{aligned} V_{LIA} &= V_r V_s \sin(\omega t + \theta_{ref}) \sin(\omega t + \theta_{sig}) \\ &= \frac{1}{2} V_r V_s \{\cos[(\omega t + \theta_{ref}) - (\omega t + \theta_{sig})] - \cos[(\omega t + \theta_{ref}) + (\omega t + \theta_{sig})]\} \\ &= \tfrac{1}{2} V_r V_s \cos(\theta_{ref} - \theta_{sig}) - \tfrac{1}{2} V_r V_s \cos(2\omega t + \theta_{ref} + \theta_{sig}) \end{aligned} \tag{1}$$

where ω is the angular laser modulation frequency $5600 \times 2\pi$, and V_r, V_s, θ_{ref} and θ_{sig} are the amplitudes and phases of the reference and Raman signals correspondingly.

The mixed signal consists of a DC component $\frac{1}{2} V_r V_s \cos(\theta_{ref} - \theta_{sig})$ and a high-frequency component $\frac{1}{2} V_r V_s \cos(2\omega t + \theta_{ref} + \theta_{sig})$. An internal low-pass filter of the LIA filters out the signal V_{LIA} and only let the DC component to pass through.

Biomedical Optics EXPRESS

The output signal of the LIA is:

$$V_{Out} = \frac{1}{2} V_r V_s \cos(\theta_{ref} - \theta_{sig}) \tag{2}$$

By locking the phase θ_{ref} to make $\cos(\theta_{ref} - \theta_{sig}) = 1$, V_{Out} can be maximized.

2.1.2. Fourier transform-Raman spectrometer

We used a Nicolet NXR 9650 Fourier Transform-Raman (FT-Raman) spectrometer (Thermo Scientific, Madison, WI, USA) to collect full range Raman spectra of the phantoms and the liver samples. The NXR 9650 system uses a 1064 nm Nd:YVO_4 excitation laser and has a spectral resolution better than 0.8 cm^{-1}. The spectrometer has a spectral range of 100-3500 cm^{-1}, which covers all the Stokes Raman characteristic peaks investigated in the previous studies [30–32]. In the current study, each sample was excited by a 300-mW laser beam, and each FT-Raman spectrum was an average of 64 consecutive scans.

2.1.3. Magnetic resonance imaging scanner

We used a 3 T pre-clinical MRI scanner (Agilent, Menlo Park, CA, USA) to provide reference quantification of fat content in the phantoms and liver samples. A quadrature radiofrequency (RF) coil (Doty Scientific, Columbia, US) with an inner diameter of 30 mm is equipped to broadcast 128-MHz RF waves and acquire data.

Since the spatial resolution is not of interest in this study, we used a simple pulse-acquire sequence to generate spectra from the bulk of the imaged volume of the sample, with a repetition time (TR) of 8 seconds, a spectral width of 10 kHz, and eight signal averages. The protons in triglyceride molecules have different proton resonance frequencies, with the most prominent fat peaks shifted downfield by approximately 3.5 ppm (420 Hz in a 3 T main field) from the water peak [35]. By adequately defining the borders of the MR peaks of triglyceride and water molecules, the fat content was calculated according to the areas of the peaks [36]:

$$Fat\ Content\ (\%) = \frac{S_{fat\ peak}}{S_{fat\ peak} + S_{water\ peak}} \times 100\% \tag{3}$$

2.2. Fat-water phantoms and livers samples

Referring to a protocol developed by Bush et al. [37], we created MRI-compatible fat-water phantoms with different fat contents by mixing a duck fat solution and an agar-water solution in varying proportions, as shown in Table 1. The duck fat solution was composed of 300 ml rendered and filtered pure duck fat (Rougié, Marieville, QC, Canada) and 3.0 ml of the oil-soluble surfactant Span 80. The water solution was composed of 300 ml deionized water, 9.0 g food-grade agar (Everland, Burnaby, BC, Canada), 0.30 g sodium benzoate, and 0.60 ml water-soluble surfactant Tween 20. Each phantom was created by adding the water solution slowly into the oil solution in an Erlenmeyer flask on a 280°C hotplate set to 1100 rpm. The heating and stirring were not stopped until the Erlenmeyer flask mixture became white, creamy, and homogenous emulsion. For fat content measurements, the emulsion was transferred to 10mm-in-diameter glass NMR tubes (SP Wilmad-Labglass, Vineland, NJ, USA).

Flash-frozen grade-B duck foie gras (aka. fatty duck liver; Rougié, Marieville, QC, Canada) and freeze-dried ordinary duck liver pieces (Pure Treats, Vaudreuil-Dorion, QC, Canada) were mixed together to create duck liver samples with a variety of fat contents. We milled mushy duck foie gras slices with pulverized freeze-dried duck liver powder in varying proportions (Table 2) to make the mixtures as homogeneous as possible. For fat content measurements, the duck liver mixtures were transferred to the NMR tubes. To compensate for the loss of free water of the freeze-dried duck liver pieces, we added deionized water into the NMR tubes and stirred the mixture to ensure homogenous absorption.

Biomedical Optics EXPRESS

Table 1. The formula of agar-water phantoms and corresponding nominal fat content

#	Agar-water solution (ml)	Duck fat solution (ml)	Nominal fat content (%)
P1	Arbitrary	0	0
P2	28.5	1.5	5
P3	27.0	3.0	10
P4	25.5	4.5	15
P5	24.0	6.0	20
P6	22.5	7.5	25
P7	21.0	9.0	30
P8	19.5	10.5	35
P9	18.0	12.0	40
P10	4.4	3.6	45
P11	15.0	15.0	50
P12	12.0	18.0	60
P13	0	Arbitrary	100

Table 2. The formula of duck liver samples

#	Fatty duck liver (mg)	Freeze-dried duck liver (mg)	Deionized water (µl)
L1	3000	0	0
L2	2800	200	400
L3	2600	400	800
L4	2400	600	1200
L5	2200	800	1600
L6	2000	1000	2000
L7	1800	1200	2400
L8	1600	1400	2800
L9	1400	1600	3200
L10	1200	1800	3600
L11	1000	2000	4000

As all the animal materials in this study were classified as food, no ethics approval was required according to the *Ethics of Animal Investigation* by the Canadian Council on Animal Care (CCAC) and the guidelines of the Dalhousie University Committee on Laboratory Animals (UCLA).

3. Results

3.1. Fat content calibration and verification of Raman signals

Duck fat phantoms P1 (i.e., pure agar-water solution) and P13 (i.e., pure duck liver fat) were used as standard samples for calibrating MRI readings and providing reference FT-Raman spectra.

Figure 2(a) and 2(b) represent MR spectra and Raman spectra of duck fat phantoms P1, P11 (50% fat content in name), P13, and duck liver sample L1 (Fatty duck liver) in the −7.0 to 0 ppm and the 2750 to 3050 cm^{-1} regions, respectively. The duck fat phantoms' highest MR water peak and fat peak emerged at approximately −1.7 ppm and −5.2 ppm, respectively. The MR fat and water peaks were broadened in the duck liver sample, owing to the inhomogeneity of the main magnetic field caused by iron in the liver. Accordingly, we defined the MR fat-peak

Biomedical Optics EXPRESS

regions as −6.5 to −5 ppm for the phantoms and −6.5 to −3.7 ppm for the liver samples. As for the MR water-peak region, we defined −3.5 to −1 ppm for the phantoms and −3.2 to 0 ppm for the liver samples. The phantoms unavoidably contain iron elements. Iron is ferromagnetic and causes inhomogeneity of magnetic field and interfere with the chemical shift [38,39]. With the increment of fat fraction, the concentration of iron elements rises in the phantoms and causes more severe inhomogeneity, MR signal dephasing, and consequently MR peak shifts.

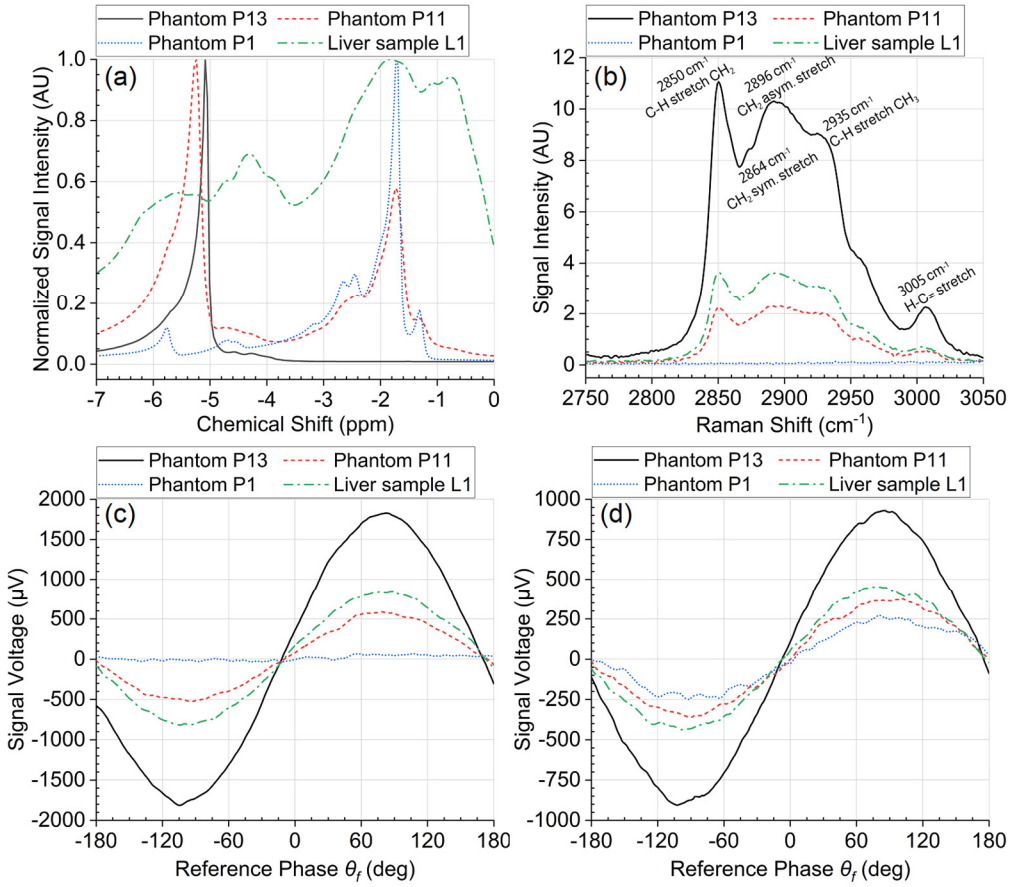

Fig. 2. (a) MR spectra, (b) FT-Raman spectra, and (c)(d) filter-based Raman system phase scans of phantom P1 (pure agar-water solution), P11 (50% fat content in name), P13 (pure duck liver fat), and liver sample L1 (Fatty duck liver) . Each data point on the phase scans is the mean value of ten repetitive collections at the same θ_{ref} with-100 ms intervals.

The FT-Raman peaks [Fig. 2(b)], as expected, did not shift with varying fat content. As the figure shows, the spectra have strong Raman characteristic peaks of lipids/proteins in the region of 2850 to 3000 cm^{-1}. Although agar has a recognizable Raman peak centered at 2926 cm^{-1} due to asymmetrical and symmetrical CH_2 stretch, the concentration of agar in our P1 phantom is low, thus no Raman peaks of agar are recognizable [40]. The intensities of the Raman peaks are positively correlated with the fat content in the phantoms and liver samples.

To calibrate our Raman system, we first placed the samples at positions where the distance from the back surface of lens L2 to the front surface of the sample is equal to L2's back focal length. By changing the LIA internal reference phase θ_{ref}, we conducted phase scans within

Biomedical Optics EXPRESS

−180 and +180 deg with a step size of 2 deg to find the maximum of signals from 1550/30-nm and 1064/3-nm channels for each of the four samples [Fig. 2(c) and 2(d)]. The maximum of the signal was observed at 87 deg phase difference. All further measurements were conducted with the LIA internal reference phase θ_{ref} locked to this value.

3.2. Performance of the filter-based Raman system

To imitate a shadowless light environment in an operating room, we used a 10000 lm LED light torch to illuminate the pure duck fat phantom P1, as Fig. 3(b) shows. Since the illuminated area is smaller than 100 cm^2, the illuminance $E_v = \frac{lumen}{Area} > 10^7\ lx$, which is larger than typical illuminance in the operating room [41]. To compare the performance of our Raman system in different background light environments, we conducted separate phase scans for P1. Figure 3(c) represents the results of the phase scans obtained from our Raman system in ordinary fluorescent light and intense LED ambient light. Each data point is a mean of ten measurements at the same area of each phantom. The mean values of the differences of all-phase signal voltages are found to be small in comparison with the informative signal voltage, especially within the phase range of 80 to 100 deg (ratio ranges from 0.022% to 0.067%), indicating that the differences are statistically negligible in both informative channels. This confirms that our Raman system is impervious to normal and strong ambient light and should be fully functional in the typical light conditions of the operating room. This is the first report of a Raman-based measurement system operating under lighting conditions because of the lock-in amplification technique.

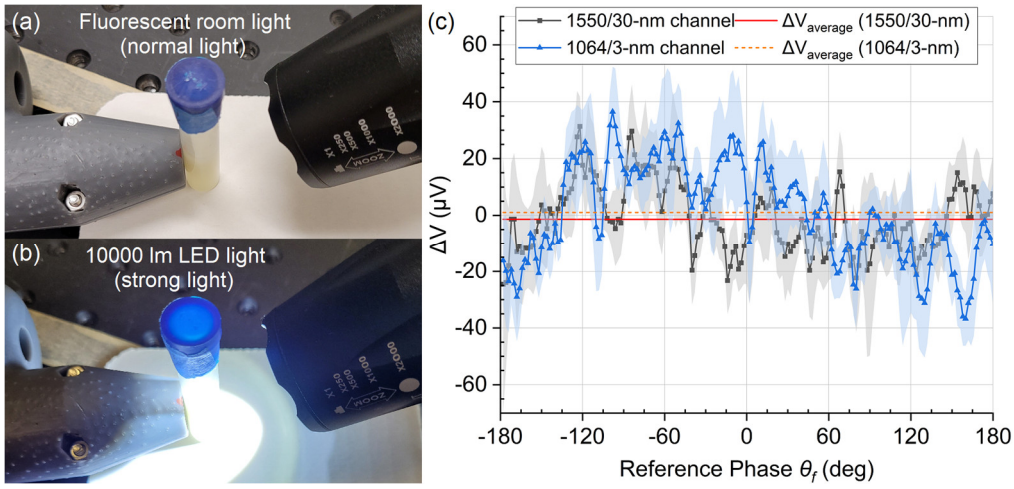

Fig. 3. Pure duck fat phantom under (a) ordinary fluorescent room light (normal light) and (b) 10000 lm LED light (strong light). (c) Voltage signal differences ($\Delta V = V_{strong\ light} - V_{normal\ light}$) of fat content measurements using the filter-based Raman system under strong and normal light. The error bars are the standard deviations over three sequential repositioning measurements (with a repetition rate of 10 and a time interval of 100 ms at each θ_{ref}).

Figure 4(a) and 4(b) show the maximum recovered signal voltages obtained from the system as a function of the MRI-estimated fat content in the duck phantoms P2-P13 and duck liver samples L1-L11 ranging from 10% to 60%, which covers the clinically relevant range of 20%−60%. The signal intensity from 1550/30-nm information channel is linearly correlated to MRI-calibrated fat content of the phantoms ($y = 11.54x - 79.10$; $r^2 = 0.980$) and the duck liver samples ($y = 11.26x - 72.43$; $r^2 = 0.964$). The signal from 1550/30-nm information channel represents Raman characteristic peaks of lipids/proteins in the 2750-3050 cm^{-1} region. The linearity has

Biomedical Optics EXPRESS

been demonstrated experimentally that the intensity of observed Raman scattering is proportional to the fat content fraction. This linear behaviour also indicates that the signal from 1550/30-nm channel can be directly translated into the fat content readings.

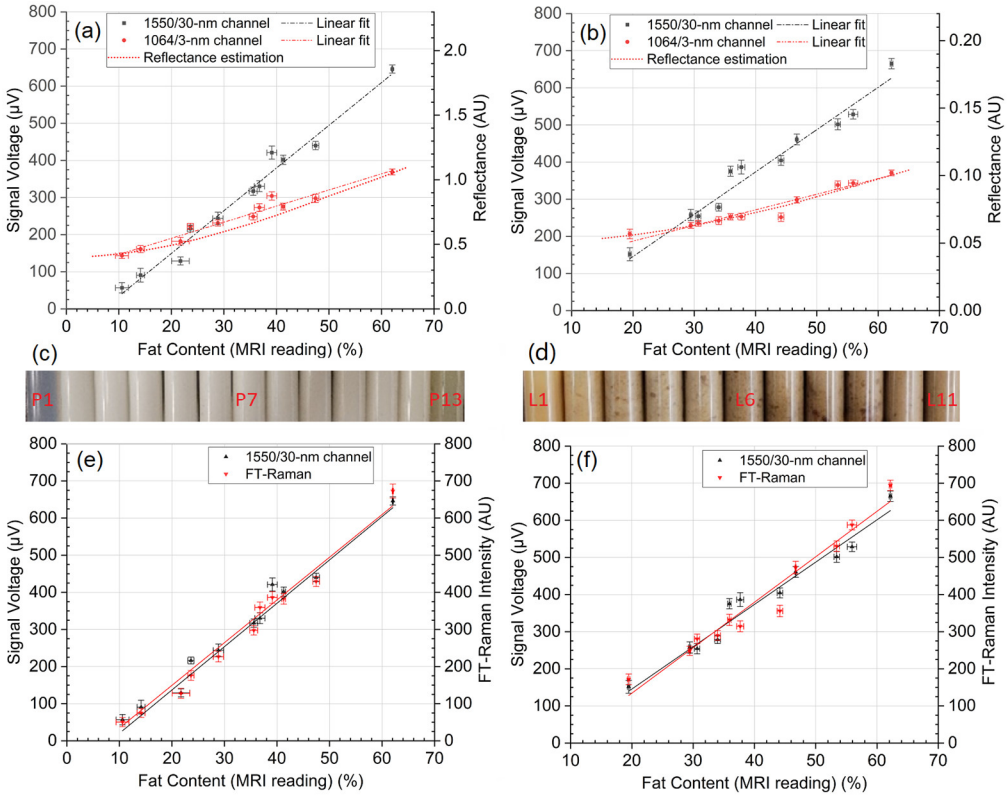

Fig. 4. Signal intensities of the 1550/30-nm channel and the 1064/3-nm channel of (a) duck fat phantoms P2-P12 (5%−60% fat content in name) and (b) duck liver samples L1-L11. (c) Duck fat phantoms P1-P13 (from left to right). (d) Duck liver samples L1-L11 (from left to right). Comparisons of signal intensities of the 1550/30-nm channel with the FT-Raman intensities using (e) duck fat phantoms P2-P12 and (f) duck liver samples L1-L11. The fat contents were calibrated using the 3 T MRI scanner. The error bars are the standard deviations over three sequential repositioning by reinserting the containers into the MRI RF coils and putting the handheld probe on different locations. The parameters of optical properties were provided by RefractiveIndex.INFO database.

The signal intensity from 1064/3-nm information channels shows the strength of diffuse reflection of the samples [Fig. 4 (a) and 4(b)]. The signal intensity curves from 1064/3-nm channel can be linearly fitted by $y = 4.37x + 102.66$ ($r^2 = 0.958$) for the phantoms and $y = 4.06x + 108.77$ ($r^2 = 0.927$) for the liver samples. However, the linear fittings lack physical significance. We used Mie theory to model the reflectance of the phantoms and the livers [42–45].

According to the research on lipid-water emulsion by Nachabé et al. [42], our water-fat phantoms [Fig. 4(c)] were assumed to be composed of 3.9 to 5.1 μm-in-diameter lipid spheres within a water medium. When the fat content increases in the water-fat phantoms, the lipid spheres become larger, and their concentration per unit volume increases. Mie theory predicted the trend seen in Fig. 4(a) and 4(b).

Biomedical Optics EXPRESS

As the liver samples [Fig. 4(d)] were made by mixing fatty livers with freeze-dried livers, the change in liver fat content was solely because of the concentration of the ballooning (fatty) liver cells. A typical fatty chicken liver has fat droplets of different sizes ranging from 6 µm to 18 µm in diameter [46]. Accordingly, we modelled our duck liver sample as 12-µm-in-diameter lipid spheres in a normal liver tissue medium. Figure 4(a) and 4(b) show that the modelled reflection curve agrees with the measured reflection from the 1064/3-nm channel, indicating that the Mie theory could explain the behaviour of diffuse reflectance of livers of various fat content.

Figure 4(e) and 4(f) provide comparisons of intensities of signals collected using our Raman system and the NXR 9650 FT-Raman spectrometer. While the signal from the Raman system was measured directly, the FT-Raman signal was obtained using the following equation:

$$I_{FT} = C \cdot \sum_{v=2879\ cm^{-1}}^{v=3012\ cm^{-1}} I_v \tag{4}$$

where C is a multiplication factor, and I_v is the intensity of light at a specific Raman shift along the width of the 1550/30-nm optical filter, i.e., between 2879 cm^{-1} and 3012 cm^{-1}. Our Raman system results agree well with the results obtained from the FT-Raman measurements, with linear correlation coefficients $r^2 = 0.986$ (phantoms) and $r^2 = 0.934$ (liver samples).

According to Xu et al., human liver is covered by a double-layer membrane Glisson's capsule, the thickness of which is generally less than 20 µm [47]. Hence, only when the penetration depth of the incident 1064 nm light is larger than 20 µm a Raman based optical system is able to measure liver fat content *in situ*. Meanwhile, although the spread of lipid in human livers is relatively homogeneous [48], the system must provide information on fat content in regions deeper than several layers of liver cells.

By placing the duck liver sample L1 beneath an optically identical cage-based Raman system, we adjusted the distance from the back surface of the lens L2 to the front cover of the sample (as Fig. 5(e)-5(g) present) and collected the signal voltages of both informative channels. When the focal plane of lens L2 is just at the top surface of the sample, we defined this focal plane position as 0. Positive values of the focal plane position indicate that the focal spot is inside the sample. In contrast, the negative values of the focal plane position indicate that the focal spot is outside the sample.

The system is theoretically able to collect scattering light from the entire depth of field; therefore, if the light does not attenuate when transmitted through the sample, the larger the sample volume is in the scope of the depth of field, the more scattered light the system collects. The area illuminated by the focal spot always has the strongest Raman scattering.

In actual liver samples the light gets attenuated. When the focal plane is moved deeper into the sample, the volume contributing to Raman scattering becomes larger; however, the focal spot area contributes less photons to Raman scattering, as the incident light is attenuated more along the sample. When the signal voltage reaches maximum, the Raman scattering increment (due to the increase of illuminated volume) counteracts the Raman scattering decrement (due to the decreased collection efficiency caused by attenuation). Therefore, the theoretic focal plane position where the 1550/30-nm channel outputs the highest signal voltage is the minimum penetration depth of the incident light. As presented in Fig. 5(a) and 5(c), the penetration depth of the 1064-nm laser is at least 1 mm into the phantoms and liver samples, proving its capability of penetrating the Glisson's capsule and cell layers near the surface.

We also observed maximum signal voltages of the 1064/3-nm channel near the 1 mm focal plane position [Fig. 5(b) and 5(d)]. However, the change of the 1064/3-nm signals was not as intense as the 1550/30-nm signals because the 1064/3-nm signals represented the intensity of diffuse reflectance of the samples. Secondary 1064-nm scattering photons of the diffuse reflectance are likely to be collected by the lenses but not likely to excite more Raman photons. A model of diffusion developed by Farrell et al [45]. could explain the diffuse reflectance of the

Biomedical Optics EXPRESS

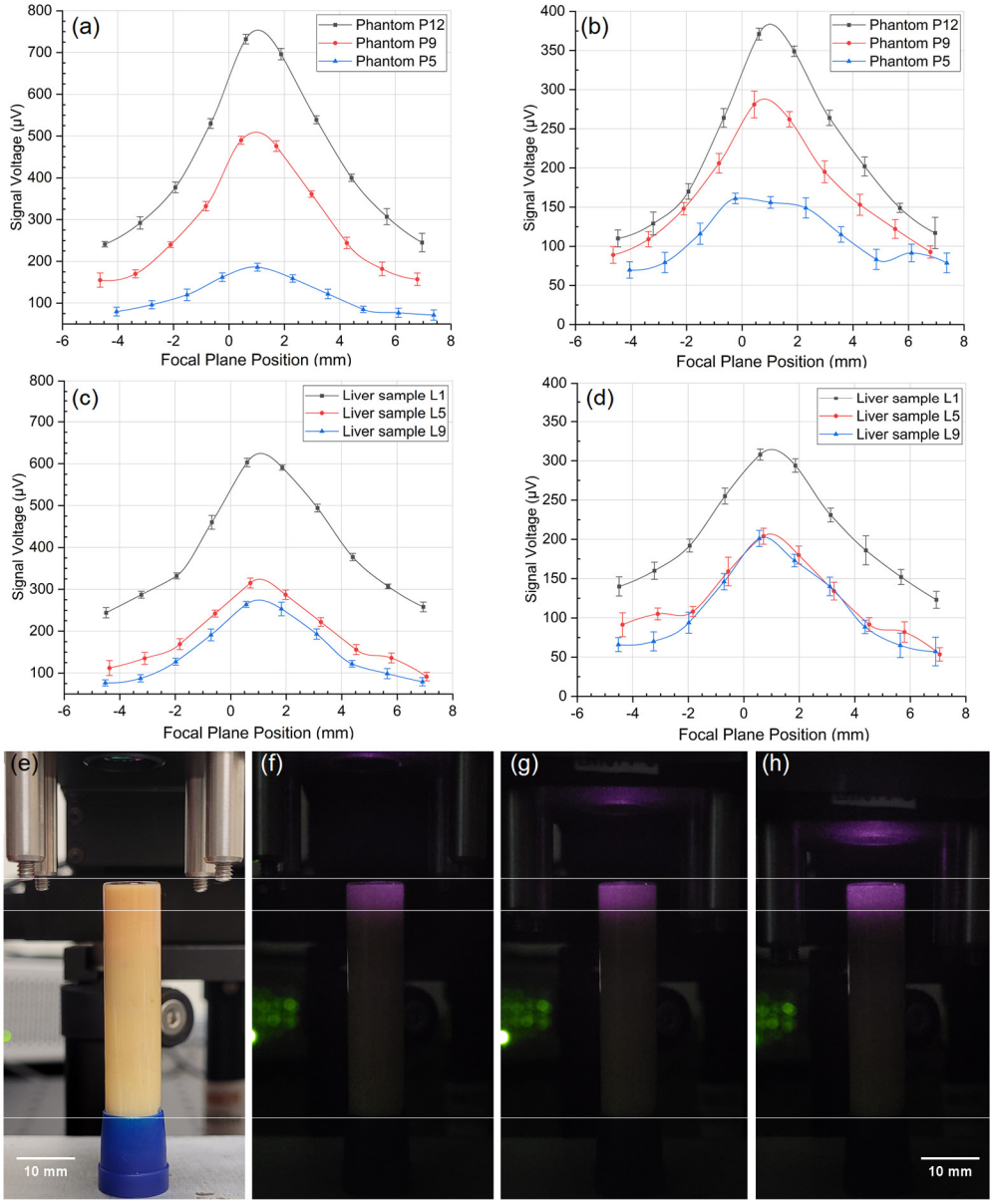

Fig. 5. Signals voltages of (a) the 1550/30-nm channel and (b) the 1064/3-nm channel vs. the focal plane position of duck fat phantoms P5 (20% fat content in name), P9 (40% fat content in name) and P12 (60% fat content in name). Signals voltages of (c) the 1550/30-nm channel and (d) the 1064/3-nm channel vs. the focal plane position of duck liver samples L1, L5 and L9. (e) Natural-color image of the duck liver sample L1 at the focal plane position of −6.35 mm. IR image of scattering of the duck liver sample L1 at the focal plane position of (f) −6.35 mm, (g) 0, and (h) 6.35 mm. The error bars are the standard deviations over 300 sequential measurements with a time interval of 100 ms.

Biomedical Optics EXPRESS

incident light from tissues; however, the theoretical explanation is not in the scope of the current study.

Although samples L5 and L9 have significant difference in 1550/30-nm signals, they yield similar signals for the 1064/3-nm channel. This is very likely due to inherent differences in the mixture of fatty and dried duck livers, including differences in equivalent lipid sizes and the size of impurities.

4. Discussion and conclusions

The need for a rapid and accurate tool for hepatic steatosis (HS) assessment of donor livers is increasing. In this work, we developed a Raman system consisting of a 1064 nm laser, a handheld probe, appropriately selected optical filters, InGaAs photodiodes, and a lock-in amplifier for real-time assessment of fat content in livers. We evaluated the performance of the system by measuring fat content in the lab-made duck fat phantoms and duck liver samples and cross-validating the results against an MRI scanner and an FT-Raman spectrometer.

The fluorescence which commonly interferes with Raman signals in tissues was avoided by using a 1064 nm excitation light. The weak signals of characteristic Raman scattering peaks and the diffuse reflectance of the samples were identified using a sensitive lock-in amplification technique.

The 1550/30-nm informative channel of the Raman system provides a signature of Raman scattering in the region of 2879 to 3012 cm^{-1}, which represents the symmetric and asymmetric stretching modes of CH_2 and CH_3 in lipid and proteins, as well as the stretching modes of = C-H bonds in lipids. The intensity of signal from 1550/30-nm information channel is linearly correlated with 3 T MRI-calibrated fat content of the phantoms ($y = 11.54x - 79.10$; $r^2 = 0.980$) and the duck liver samples ($y = 11.26x - 72.43$; $r^2 = 0.964$). The signal voltages agree with the Raman intensity provided by the FT-Raman spectrometer, with linear correlation coefficients $r^2 = 0.986$ (phantoms) and $r^2 = 0.934$ (liver samples). Compared with a moderate resolution FT-Raman system, our Raman system has clear advantages as it is smaller in size, simple in terms of design and data analysis, and fifteen-fold cheaper ($5,000 vs. $75,000).

The signal from the 1064/3-nm channel represents the intensity of diffuse reflection of the samples. The signal intensity vs. MRI-calibrated fat content curves from 1064/3-nm channel can be linearly fitted by $y = 4.37x + 102.66$ ($r^2 = 0.958$) for the phantoms and $y = 4.06x + 108.77$ ($r^2 = 0.927$) for the liver samples. The Mie theorey could explain the reflectance, and it is more suitable for the liver samples. Since the physical mechanisms of Raman scattering and diffuse reflection are different, the 1550/30-nm channel, which was shown to have stronger signal voltages and better linearity, can act as a major channel, and the 1064/3-nm channel can provide cross-validations of the liver fat content readings in the clinically relevant range.

Overcoming Raman spectroscopy's susceptibility to background light interference, our Raman system performs consistently in the normal and the strong ambient light, which is confirmed by the phase-scan results. This is because the fractions of 1064-nm and 1550-nm light are negligible in the emission spectra of fluorescent and LED light sources, and more importantly, the lock-in detection subtracts periodic voltages signal at 5600 Hz and blocks voltage signals of fluorescent and LED light at 50–60 Hz, in together with other non-periodic background light.

The system achieves a penetration depth of at least 1 mm into the phantoms and liver samples, which enables collecting information from a considerable volume of liver parenchyma beneath the double-layer Glisson's capsule. These two features make the system capable of *in-situ* diagnosis of the degree of HS and the liver fat content in the operating room under bright LED surgical light. Compared with the volume of livers, the penetration depth is shallow. Fortunately, to some extent, there is homogeneity of hepatic lipid distribution in most cases of NAFLD, which makes

Biomedical Optics EXPRESS

the superficial measurement by our customized probe representative of intrahepatic fat content [49–51].

Glisson's capsule consists of connective tissue of typical Type-I collagen fibrils [52]. The absorption of type I collagen to light above 1064 nm is in the range of 0.04 to 2.5 cm^{-1} [53]. Considering the thickness of which is generally less than 20 µm, the absorption of the Glisson's capsule is reasonably negligible [47].

The laser fluence will be influenced by scattering and absorption processes. The structure of the tissue (e.g., lipid particle size, cell size, and collagen) and its photoactive components (e.g., bilirubin) will ultimately determine the minimum penetration depth.

This is the first report of a Raman-based measurement system operating under normal lighting conditions because of the use of a lock-in amplification technique. This technique enables analyzing signals of characteristic Raman peaks without a spectrometer. Our optical filter-based Raman system has many advantages over surgeon's visual inspection and other non-invasive tools. It is accurate, non-invasive, cost effective, fast, and expected to be easy to use in an operating room. It can provide an objective assessment of the liver fat content from which liver transplant surgeons could benefit to make more confident estimations about the risks of liver grafts. The next step of this study will be examining *ex situ* and *in vivo* human livers in transplant centres.

Funding. Mitacs (39329); Sprinboard Atlantic (36852); Innovcorp (R34343).

Acknowledgements. The authors thank James Rioux for collecting and analyzing MRI data, Michel Johnson for providing access to the FT-Raman system, Andy George for providing a diamond saw, and Benjamin Hansson for constructive discussions and helpful comments on the manuscript. The authors also thank Thorlabs Inc. for providing CAD models of optical elements and Scott Prahl for providing the interactive Mie Scattering Calculator.

Disclosures. The authors HG, ABT, IPJA, HZ, and KCH have filed a provisional patent application, and they stand to benefit should the patent be awarded.

Data availability. Data underlying the results presented in this paper are not publicly available at this time but may be obtained from the authors upon reasonable request.

Supplemental document. See Supplement 1 for supporting content.

References

1. B. Domínguez-Gil, "International Figures On Organ, Tissue & Hematopoietic Stemcell Donation & Transplantation Activities 2020," http://www.transplant-observatory.org/wp-content/uploads/2021/09/V4.pdf.
2. C. Tschuor, A. Ferrarese, C. Kuemmerli, P. Dutkowski, P. Burra, P. A. Clavien, J. Lendoire, O. Imventarza, M. Crawford, W. Andraus, L. A. C. D'Albuquerque, R. Hernandez-Alejandro, M. K. Dokus, K. Tomiyama, S. Zheng, G. J. Echeverri, P. Taimr, J. Fronek, M. de Rosner-van Rosmalen, S. Vogelaar, M. Lesurtel, J. Y. Mabrut, S. Nagral, F. Kakaei, S. A. Malek-Hosseini, H. Egawa, A. Contreras, J. Czerwinski, T. Danek, H. Pinto-Marques, S. V. Gautier, A. Monakhov, E. Melum, B. G. Ericzon, K. J. Kang, M. S. Kim, P. Sanchez-Velazquez, C. E. Oberkofler, B. Müllhaupt, M. Linecker, D. Eshmuminov, L. F. Grochola, Z. Song, P. Kambakamba, C. L. Chen, M. Haberal, S. Yilmaz, I. A. C. Rowe, and P. Kron, "Allocation of liver grafts worldwide – Is there a best system?" J. Hepatol. **71**(4), 707–718 (2019).
3. L. Bicudo de Oliveira, E. Riccetto, and I. de Fátima Santana Ferreira Boin, "Prevalence and profile of discarded liver donors in a tertiary health service in Brazil From 2015 to 2018," Transplant. Proc. **52**(5), 1251–1255 (2020).
4. D. J. Carpenter, M. C. Chiles, E. C. Verna, K. J. Halazun, J. C. Emond, L. E. Ratner, and S. Mohan, "Deceased brain dead donor liver transplantation and utilization in the united states: nighttime and weekend effects," Transplantation **103**(7), 1392–1404 (2019).
5. S. Masson, R. Taylor, J. Whitney, A. Adair, M. Attia, P. Gibbs, T. Grammatikopoulos, J. Isaac, A. Marshall, D. Mirza, A. Prachalias, S. Watson, D. Manas, J. Forsythe, and D. Thorburn, "A coordinated national UK liver transplant program response, prioritizing waitlist recipients with the highest need, provided excellent outcomes during the first wave of the COVID-19 pandemic," Clin. Transplant. **36**(4), e14563 (2022).
6. F. Dengu, S. H. Abbas, G. Ebeling, and D. Nasralla, "Normothermic machine perfusion (NMP) of the liver as a platform for therapeutic interventions during ex-vivo liver preservation: a review," J. Clin. Med. **9**(4), 1046 (2020).
7. P. Angulo, "Nonalcoholic fatty liver disease and liver transplantation," Liver Transplant. **12**(4), 523–534 (2006).
8. L. McCormack, P. Dutkowski, A. M. El-Badry, and P. A. Clavien, "Liver transplantation using fatty livers: Always feasible?" J. Hepatol. **54**(5), 1055–1062 (2011).
9. E. E. Powell, V. W. S. Wong, and M. Rinella, "Non-alcoholic fatty liver disease," Lancet **397**(10290), 2212–2224 (2021).
10. C. J. Imber, S. D. St. Peter, A. Handa, and P. J. Friend, "Hepatic steatosis and its relationship to transplantation," Liver Transplant. **8**(5), 415–423 (2002).

Biomedical Optics EXPRESS

11. M. J. J. Chu, A. J. Dare, A. R. J. Phillips, and A. S. J. R. Bartlett, "Donor hepatic steatosis and outcome after liver transplantation: a systematic review," J. Gastrointest. Surg. **19**(9), 1713–1724 (2015).
12. M. Selzner and P. A. Clavien, "Fatty liver in liver transplantation and surgery," Semin. Liver Dis. **21**(01), 105–114 (2001).
13. T. C. L. Wong, J. Y. Y. Fung, K. S. H. Chok, T. T. Cheung, A. C. Y. Chan, W. W. Sharr, W. C. Dai, S. C. Chan, and C. M. Lo, "Excellent outcomes of liver transplantation using severely steatotic grafts from brain-dead donors," Liver Transplant. **22**(2), 226–236 (2016).
14. T. Ivanics, P. Abreu, E. De Martin, and G. Sapisochin, "Changing trends in liver transplantation: challenges and solutions," Transplantation **105**(4), 743–756 (2021).
15. A. Nocito, A. M. El-Badry, and P. A. Clavien, "When is steatosis too much for transplantation?" J. Hepatol. **45**(4), 494–499 (2006).
16. J. A. Steggerda, M. B. Bloom, M. Noureddin, T. V. Brennan, T. Todo, N. N. Nissen, A. S. Klein, and I. K. Kim, "Higher thresholds for the utilization of steatotic allografts in liver transplantation: Analysis from a U.S. national database," PLoS One **15**(4), e0230995 (2020).
17. K. P. Croome, D. D. Lee, S. Croome, R. Chadha, D. Livingston, P. Abader, A. P. Keaveny, and C. B. Taner, "The impact of postreperfusion syndrome during liver transplantation using livers with significant macrosteatosis," Am. J. Transplant **19**(9), 2550–2559 (2019).
18. P. Dutkowski, C. E. Oberkofler, K. Slankamenac, M. A. Puhan, E. Schadde, B. Müllhaupt, A. Geier, and P. A. Clavien, "Are there better guidelines for allocation in liver transplantation?: A novel score targeting justice and utility in the model for end-stage liver disease era," Ann. Surg. **254**(5), 745–754 (2011).
19. H. Mergental, R. W. Laing, A. J. Kirkham, M. T. P. R. Perera, Y. L. Boteon, J. Attard, D. Barton, S. Curbishley, M. Wilkhu, D. A. H. Neil, S. G. Hübscher, P. Muiesan, J. R. Isaac, K. J. Roberts, M. Abradelo, A. Schlegel, J. Ferguson, H. Cilliers, J. Bion, D. H. Adams, C. Morris, P. J. Friend, C. Yap, S. C. Afford, and D. F. Mirza, "Transplantation of discarded livers following viability testing with normothermic machine perfusion," Nat. Commun. **11**(1), 2939 (2020).
20. L. I. Mazilescu, M. Selzner, and N. Selzner, "Defatting strategies in the current era of liver steatosis," JHEP Reports **3**(3), 100265 (2021).
21. H. Yersiz, C. Lee, F. M. Kaldas, J. C. Hong, A. Rana, G. T. Schnickel, J. A. Wertheim, A. Zarrinpar, V. G. Agopian, J. Gornbein, B. V. Naini, C. R. Lassman, R. W. Busuttil, and H. Petrowsky, "Assessment of hepatic steatosis by transplant surgeon and expert pathologist: A prospective, double-blind evaluation of 201 donor livers," Liver Transplant. **19**(4), 437–449 (2013).
22. K. Karayalcin, D. F. Mirza, R. F. Harrison, R. F. Da Silva, S. G. Hubscher, A. D. Mayer, J. A. C. Buckels, and P. McMaster, "The role of dynamic and morphological studies in the assessment of potential liver donors," Transplantation **57**(9), 1323–1327 (1994).
23. S. Saadeh, Z. M. Younossi, E. M. Remer, T. Gramlich, J. P. Ong, M. Hurley, K. D. Mullen, J. N. Cooper, and M. J. Sheridan, "The utility of radiological imaging in nonalcoholic fatty liver disease," Gastroenterology **123**(3), 745–750 (2002).
24. J. R. Van Werven, H. A. Marsman, A. J. Nederveen, N. J. Smits, F. J. Ten Kate, T. M. Van Gulik, and J. Stoker, "Assessment of hepatic steatosis in patients undergoing liver resection: Comparison of US, CT, T1-weighted dual-echo MR imaging, and point-resolved 1H MR spectroscopy," Radiology **256**(1), 159–168 (2010).
25. M. Cesaretti, P. Addeo, L. Schiavo, R. Anty, and A. Iannelli, "Assessment of liver graft steatosis: where do we stand?" Liver Transplant. **25**(3), 500–509 (2019).
26. Y. M. Wu, H. C. Chen, W. T. Chang, J. W. Jhan, H. L. Lin, and I. Liau, "Quantitative assessment of hepatic fat of intact liver tissues with coherent anti-stokes Raman scattering microscopy," Anal. Chem. **81**(4), 1496–1504 (2009).
27. Y. Adkins, I. W. Schie, D. Fedor, A. Reddy, S. Nguyen, P. Zhou, D. S. Kelley, and J. Wu, "A novel mouse model of nonalcoholic steatohepatitis with significant insulin resistance," Lab. Invest. **93**(12), 1313–1322 (2013).
28. K. Majzner, K. Kochan, N. Kachamakova-Trojanowska, E. Maslak, S. Chlopicki, and M. Baranska, "Raman imaging providing insights into chemical composition of lipid droplets of different size and origin: in hepatocytes and endothelium," Anal. Chem. **86**(13), 6666–6674 (2014).
29. N. Golse, C. Cosse, M. A. Allard, A. Laurenzi, M. Tedeschi, N. Guglielmo, E. Fernandez-Sevilla, M. Robert, B. Tréchot, D. Pietrasz, G. Pittau, O. Ciacio, A. Sa Cunha, D. Castaing, D. Cherqui, R. Adam, D. Samuel, M. Sebagh, and E. Vibert, "Evaluation of a micro-spectrometer for the real-time assessment of liver graft with mild-to-moderate macrosteatosis: A proof of concept study," J. Hepatol. **70**(3), 423–430 (2019).
30. K. C. Hewitt, J. Ghassemi Rad, H. C. McGregor, E. Brouwers, H. Sapp, M. A. Short, S. B. Fashir, H. Zeng, and I. P. Alwayn, "Accurate assessment of liver steatosis in animal models using a high throughput Raman fiber optic probe," Analyst **140**(19), 6602–6609 (2015).
31. M. Z. Pacia, K. Czamara, M. Zebala, E. Kus, S. Chlopicki, and A. Kaczor, "Rapid diagnostics of liver steatosis by Raman spectroscopy via fiber optic probe: a pilot study," Analyst **143**(19), 4723–4731 (2018).
32. I. J. Pence, C. A. Patil, C. A. Lieber, and A. Mahadevan-Jansen, "Discrimination of liver malignancies with 1064 nm dispersive Raman spectroscopy," Biomed. Opt. Express **6**(8), 2724 (2015).
33. K. Czamara, K. Majzner, M. Z. Pacia, K. Kochan, A. Kaczor, and M. Baranska, "Raman spectroscopy of lipids: a review," J. Raman Spectrosc. **46**(1), 4–20 (2015).

Biomedical Optics EXPRESS

34. K. Kochan, K. M. Marzec, K. Chruszcz-Lipska, A. Jasztal, E. Maslak, H. Musiolik, S. Chłopicki, and M. Baranska, "Pathological changes in the biochemical profile of the liver in atherosclerosis and diabetes assessed by Raman spectroscopy," Analyst **138**(14), 3885–3890 (2013).
35. T. A. Bley, O. Wieben, C. J. François, J. H. Brittain, and S. B. Reeder, "Fat and water magnetic resonance imaging," J. Magn. Reson. Imaging **31**(1), 4–18 (2010).
36. D. Pasanta, K. T. Htun, J. Pan, M. Tungjai, S. Kaewjaeng, H. Kim, J. Kaewkhao, and S. Kothan, "Magnetic Resonance Spectroscopy of Hepatic Fat from Fundamental to Clinical Applications," *Diagnostics* (Basel) 11, (2021).
37. E. C. Bush, A. Gifford, C. L. Coolbaugh, T. F. Towse, B. M. Damon, and E. B. Welch, "Fat-Water Phantoms for Magnetic Resonance Imaging Validation: A Flexible and Scalable Protocol," J. Vis. Exp. **139**(139), 57704 (2018).
38. S. S. Lee, Y. Lee, N. Kim, S. W. Kim, J. H. Byun, S. H. Park, M. G. Lee, and H. K. Ha, "Hepatic fat quantification using chemical shift MR imaging and MR spectroscopy in the presence of hepatic iron deposition: validation in phantoms and in patients with chronic liver disease," J. Magn. Reson. Imaging **33**(6), 1390–1398 (2011).
39. J. P. Kühn, D. Hernando, B. Mensel, P. C. Krüger, T. Ittermann, J. Mayerle, N. Hosten, and S. B. Reeder, "Quantitative Chemical Shift-Encoded MRI Is an Accurate Method to Quantify Hepatic Steatosis," J. Magn. Reson. Imaging **39**(6), 1494–1501 (2014).
40. T. López, M. Picquart, G. Aguirre, G. Arriola, Y. Freile, D. H. Aguilar, P. Quintana, J. J. Alvarado-Gil, and F. M. Vargas-Luna, "Thermal Characterization of Agar Encapsulated in TiO2 Sol–Gel," Int. J. Thermophys. **25**(5), 1483–1493 (2004).
41. H. Hemphälä, W. Osterhaus, P. A. Larsson, J. Borell, and P. Nylén, "Towards better lighting recommendations for open surgery:," https://doi.org/10.1177/1477153520903355 52, 856–882 (2020).
42. R. Nachabe, B. H. W. Hendriks, A. E. Desjardins, M. van der Voort, M. B. van der Mark, and H. J. C. M. Sterenborg, "Estimation of lipid and water concentrations in scattering media with diffuse optical spectroscopy from 900 to 1600 nm," J. Biomed. Opt. **15**(3), 037015 (2010).
43. K. Soga, K. Okubo, M. Umezawa, M. Kamimura, N. Hosokawa, N. Ohtani, T. Kamiya, and Y. Kitagawa, "Visualization of quantitative lipid distribution in mouse liver through near-infrared hyperspectral imaging," Biomed. Opt. Express **12**(2), 823–835 (2021).
44. I. Y. Yanina, E. N. Lazareva, and V. V. Tuchin, "Refractive index of adipose tissue and lipid droplet measured in wide spectral and temperature ranges," Appl. Opt. **57**(17), 4839 (2018).
45. T. J. Farrell, M. S. Patterson, and B. Wilson, "A diffusion theory model of spatially resolved, steady-state diffuse reflectance for the noninvasive determination of tissue optical properties in vivo," Med. Phys. **19**(4), 879–888 (1992).
46. Y. H. Zhang, Z. Liu, R. R. Liu, J. Wang, M. Q. Zheng, Q. H. Li, H. X. Cui, G. P. Zhao, and J. Wen, "Alteration of Hepatic Gene Expression along with the Inherited Phenotype of Acquired Fatty Liver in Chicken," Genes **9**(4), 199 (2018).
47. S. Xu, C. H. Kang, X. Gou, Q. Peng, J. Yan, S. Zhuo, C. L. Cheng, Y. He, Y. Kang, W. Xia, P. T. C. So, R. Welsch, J. C. Rajapakse, and H. Yu, "Quantification of liver fibrosis via second harmonic imaging of the Glisson's capsule from liver surface," J. Biophotonics **9**(4), 351–363 (2016).
48. S. M. Abd El-Kader and E. M. S. El-Den Ashmawy, "Non-alcoholic fatty liver disease: The diagnosis and management," World J. Hepatol. **7**(6), 846 (2015).
49. E. L. Thomas, G. Hamilton, N. Patel, R. O'Dwyer, C. J. Doré, R. D. Goldin, J. D. Bell, and S. D. Taylor-Robinson, "Hepatic triglyceride content and its relation to body adiposity: a magnetic resonance imaging and proton magnetic resonance spectroscopy study," Gut **54**(1), 122–127 (2005).
50. J. Machann, C. Thamer, B. Schnoedt, N. Stefan, H. U. Haring, C. D. Claussen, A. Fritsche, and F. Schick, "Hepatic lipid accumulation in healthy subjects: a comparative study using spectral fat-selective MRI and volume-localized 1H-MR spectroscopy," Magn. Reson. Med. **55**(4), 913–917 (2006).
51. F. Springer, J. Machann, C. D. Claussen, F. Schick, and N. F. Schwenzer, "Liver fat content determined by magnetic resonance imaging and spectroscopy," World J. Gastroenterol. **16**(13), 1560 (2010).
52. G. B. Chapman and D. A. Eagles, "Ultrastructural features of Glisson's capsule and the overlying mesothelium in rat, monkey and pike liver," Tissue Cell **39**(5), 343–351 (2007).
53. S. K. V. Sekar, I. Bargigia, A. D. Mora, P. Taroni, A. Ruggeri, A. Tosi, A. Pifferi, and A. Farina, "Diffuse optical characterization of collagen absorption from 500 to 1700nm," J. Biomed. Opt. **22**(1), 015006 (2017).